Dynamics of an Expanding Circular Fault

Article *in* Bulletin of the Seismological Society of America · June 1976

1 author:

Some of the authors of this publication are also working on these related projects:

Project   Dynamic source inversion of Mexican earthquakes View project

Project   Evaluation of tsunami hazard and coastal free oscillation in France View project

DYNAMICS OF AN EXPANDING CIRCULAR FAULT

BY RAUL MADARIAGA

ABSTRACT

We study a plane circular model of a frictional fault using numerical methods. The model is dynamic since we specify the effective stress at the fault. In one model we assume that the fault appears instantaneously in the medium; in another, that the rupture nucleates at the center and that rupture proceeds at constant subsonic velocity until it suddenly stops. The total source slip is larger at the center and the rise time is also longer at the center of the fault. The dynamic slip overshoots the static slip by 15 to 35 per cent. As a consequence, the stress drop is larger than the effective stress and the apparent stress is less than one half the effective stress.

The far-field radiation is discussed in detail. We distinguish three spectral regions. First, the usual constant low-frequency level. Second, an intermediate region controlled by the fault size and, finally, the high-frequency asymptote. The central region includes the corner frequency and is quite complicated. The corner frequency is shown to be inversely proportional to the width of the far-field displacement pulse which, in turn, is related to the time lag between the stopping phases. The average corner frequency of S waves $v_0{}^s$ is related to the final source radius, a, by $v_0{}^s = 0.21 \, \beta/a$. The corner frequency of P waves is larger than $v_0{}^s$ by an average factor of 1.5.

INTRODUCTION

A shallow earthquake is usually modeled as the spontaneous rupture on a fault produced by a sudden loss of traction due to frictional instability. The dynamic consequences of this model are difficult to assess due to serious analytical problems that arise when studying even the simplest antiplane models. In the last 10 years a series of dynamic crack problems have been solved analytically: Kostrov (1964) solved the self-similar circular shear crack; Kostrov (1966) solved the unstable semi-infinite antiplane shear crack; Burridge and co-workers (1969, 1973, 1974) and Richards (1973) studied the elliptical self-similar crack; and Freund (1972a) and Kostrov (1974b) solved the semi-infinite plane crack. All of these problems have no intrinsic length scale since the fault is either semi-infinite or it expands self-similarly forever. In order to study finite sources we would have to solve multiple diffraction problems which at best would lead to a series of multiple integrals. The computation of such a series would probably require as much effort as using a fully numerical method from the outset (Kostrov, 1974b).

A natural alternative is to use numerical techniques. Burridge (1969) used a numerical solution of the integral equation representation of the problem to solve some finite plane and antiplane cracks. A similar method has been used by Hamano (1974). Finite difference or finite element methods have also been used for the same problems by Dieterich (1974), Hanson et al. (1974) and Andrews (1975). It is rather unfortunate that some of these methods generate large spurious oscillations of the stress and particle velocity fields. The particle velocity and stress have a very important role in crack problems since they control the boundary conditions at the source, while the slip velocity on the fault determines the far-field radiation. We have recently developed new finite difference methods that minimize the instabilities and numerical dispersion produced by the mixed boundary conditions (Madariaga, 1974). A modification of this method will be used to study faults with circular symmetry.

We study the elasto-dynamic problem of a plane circular shear fault that either appears instantaneously or expands at a constant subsonic rupture velocity until it stops. In the interior of the fault we specify a dynamic stress drop from a constant initial prestress to the kinetic frictional stress. The prescription of dynamic stress drop (effective stress) in the fault distinguishes this problem from the kinematic models of Savage (1966, 1974), where slip was arbitrarily specified. The models to be studied are certainly quite simple, and are at best a first approximation to the events in a real fault, yet they include most of the parameters usually used by seismologists to describe seismic sources. Our purpose is to study the way these parameters determine the source slip function, the far-field radiation and the overall physics of the relaxation phenomenon.

THE CIRCULAR FAULT MODEL

We study two models of plane circular faults. In the first model, rupture occurs instantaneously inside a circle of radius a. In the second, more realistic model, rupture nucleates at a point, and a circular rupture front expands at a constant subsonic rupture velocity v_R. Fault growth stops instantaneously at time $t_r = a/v_R$ leaving a final rupture zone of radius a. The geometry of the problem is described in Figure 1. The nucleation point is at the origin of coordinates and the fault is part of the $(x–y)$ coordinate plane. The fault is completely embedded in an infinite homogeneous, isotropic elastic medium so that the displacement $\vec{u}$ satisfies the equation of motion

$$\rho \frac{\partial^2}{\partial t^2} \vec{u} = (\lambda + \mu)\nabla\nabla\cdot\vec{u} + \mu\nabla^2\vec{u} \tag{1}$$

where λ and μ are the elastic constants and ρ is the density of the medium.

A homogeneous state of stress σ_{ij}^0 exists before rupture initiation. Stress on the fault $(z = 0)$ may be separated into a normal stress σ_{zz}^0 and a shear stress $\sigma_{xz}^0 = \tau^0$. The shear stress is assumed to be sufficient to initiate rupture at the fault. Within the ruptured part of the fault, slip is resisted by kinetic friction between the sides of the fault. Assuming a constant kinematic friction coefficient μ_k (independent of position, time, slip and slip velocity), the frictional stress on the fault is

$$\vec{T}^+ = -\mu_k\sigma_{zz}^0\vec{\Delta\dot{u}}/|\Delta\dot{u}|. \tag{2}$$

This is the frictional stress acting on the upper side (+ side) of the fault; the stress on the lower side (− side) of the fault has the opposite sign. $\vec{\Delta u} = \vec{u}^+ - \vec{u}^-$ is the slip velocity between adjacent points across the fault. The minus sign in (2) indicates that

friction resists slip. Let ψ be the angle between the slip velocity vector and the x axis, then

$$\vec{\Delta\dot{u}} = |\Delta\dot{u}|(\hat{\imath}\cos\psi + \hat{\jmath}\sin\psi) \tag{3}$$

where $\hat{\imath}$ and $\hat{\jmath}$ are the unit vectors in the x and y directions, respectively. Equation (2) may now be rewritten in the form

$$\vec{T}^{+} = -\tau^{k}(\hat{\imath}\cos\psi + \hat{\jmath}\sin\psi) \tag{4}$$

where $\tau^{k} = \mu_{k}\sigma_{zz}^{0}$.

The solution of the problem requires solving (1) with the boundary conditions (4) at the fault and the condition $\sigma_{ij} \to \sigma_{ij}^{0}$ at infinity. As is usual in crack theory, we use the
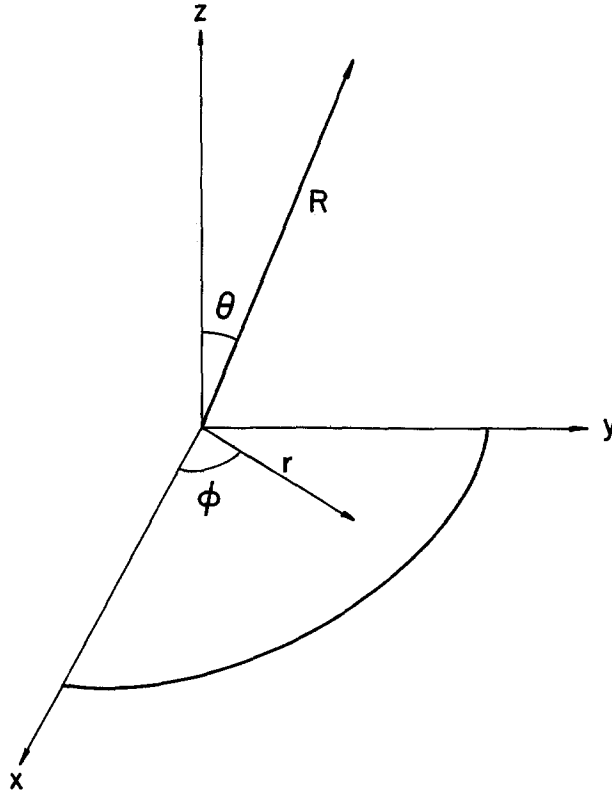

FIG. 1. General configuration of the coordinate systems used in the text. The fault is contained in the $(x\ y)$ plane.

superposition principle to subtract the initial static state from the dynamic solution. Designating the new solution with the index one, we have $\vec{u}^{1} = \vec{u} - \vec{u}^{0}$ for the displacements and $\sigma_{ij}^{1} = \sigma_{ij} - \sigma_{ij}^{0}$ for the stresses. The equation of motion for u^{1} is still (1) but the boundary conditions at infinity become $\sigma_{ij}^{1} \to 0$. The boundary condition on the $(+)$ side of the fault becomes

$$\vec{T}^{1+} = (\tau^{0} - \tau^{k}\cos\psi)\hat{\imath} - \tau^{k}\sin\psi\hat{\jmath} \tag{5}$$

and the opposite sign for $\vec{T}^{1-}$. Thus, if slip were not parallel to the x axis, the stress $\vec{T}^{1+}$ would not be parallel to the initial stress. We would have to find a solution letting ψ be

an unknown function and then solve for ψ from the boundary condition (2). This complicated boundary condition is a consequence of the nonlinearity of friction and it appears only in three-dimensional problems. Two of the problems solved analytically yield contradictory results; in the case of the subsonic self-similar circular crack, Kostrov (1964) found that $\psi \equiv 0$, while $\psi \neq 0$ in the transonic case (Burridge and Levy, 1974). However we can make a heuristic argument that $\Delta \dot{u}_y$ should be rather small. In fact, while $\Delta \dot{u}_x$ in (3) has the same sign as T_x^{1+}, $\Delta \dot{u}_y$ is opposed by T_y^{1+} so that it would probably be different from zero only as a result of some distortion of the fault slip due to the rupture front. In terms of the original problem, while $\Delta \dot{u}_x$ results from stress relaxation, $\Delta \dot{u}_y$ actually loads the medium further. Here we assumed that $\psi \equiv 0$ and then checked that the numerical solution for $\Delta \dot{u}_y$ is indeed negligible. In the initial, self-similar (v_r constant) part of the rupture, we found $\Delta \dot{u}_y \approx 0$ in agreement with the exact solution. After rupture stopped, $\Delta \dot{u}_y$ was always less than 10 per cent of $\Delta \dot{u}_x$ near the edge of the fault and negligible in the interior of the fault. Since the precision of the numerical method is not better than 10 per cent near the edge of the fault, we shall assume in the following that $\psi = 0$.

The problem can be simplified further noting the following symmetry about the $z = 0$ plane: σ_{zx}^1, σ_{zy}^1, and u_z^1 are even, while σ_{zz}^1, u_x^1, and u_y^1 are odd. This reduces the problem to the solution of (1) in the upper half-space ($z > 0$) subject to the boundary conditions on $z = 0$

$$\sigma_{zx}^1 = \tau_e \qquad\qquad \text{for } r < \min(v_R t, a)$$

$$\sigma_{zy}^1 = 0 \qquad\qquad \text{for } r < \min(v_R t, a)$$

$$u_x^1 = u_y^1 = 0 \qquad\qquad \text{for } r > \min(v_R t, a)$$

and

$$\sigma_{zz}^1 = 0 \qquad\qquad \text{for all } r. \qquad (6)$$

Where $\tau_e = \tau^0 - \tau^k$ is the dynamic stress drop or effective stress as defined by Brune (1970). The index 1 will be dropped in the following in order to simplify the notation.

The problem requires some additional physical assumptions (Kostrov, 1964) because of the singularities that appear at $r = v_R t$ due to the abrupt change in boundary conditions. In principle these stress concentrations would be inadmissible since they violate the assumptions of finite stress and infinitesimal strains of linear elasto-dynamics. Kostrov et al. (1970) and Freund (1972b) have demonstrated that these singularities are associated with the energy absorbed at the rupture front as it advances. This energy flow provides the fracture energy to advance the rupture front. In order for the energy to be finite, the stresses and slip velocities should have at most square-root singularities at the edge of the fault. This last condition is necessary to obtain a unique solution to the problem (Kostrov, 1964).

We shall solve the circular fault problem assuming constant subsonic rupture velocity with the understanding that the strength of the stress singularities is a measure of the fracture energy available. In fact, the fracture energy is an independent physical parameter which determines the rupture velocity as done by Kostrov (1966) and Ida (1973) for semi-infinite cracks. This would be extremely difficult to implement in the numerical method we have used, so that we have fixed the rupture velocity.

REDUCTION TO A TWO-DIMENSIONAL PROBLEM

The geometry of the fault, described in Figure 1, suggests cylindrical coordinates (r, ϕ, z) as the most appropriate system to study the problem. Rewriting the boundary

conditions (6) we find on $z = 0$

$$\sigma_{rz} = -\tau_e \cos\phi \qquad\qquad r < \min{(v_R t, a)},$$

$$\sigma_{\phi z} = \tau_e \sin\phi \qquad\qquad r < \min{(v_R t, a)},$$

$$u_r = u_\phi = 0 \qquad\qquad r > \min{(v_R t, a)}, \quad (7)$$

and

$$\sigma_{zz} = 0 \qquad\qquad \text{for all r.}$$

These boundary conditions have a simple sinusoidal azimuthal dependence. Therefore, we can use the separability of the angular variable to simplify the solution. In fact only terms with $\cos\phi$ and $\sin\phi$ will appear in the solution, which is of the form

$$u_r = u(r, z, t) \cos\phi$$

$$u_z = w(r, z, t) \cos\phi$$

$$u_\phi = v(r, z, t) \sin\phi \qquad\qquad (8)$$

Inserting (8) in (1) we may obtain a system of three coupled second-order P.D.E. for u, v, and w in the variables r, z, and t. This reduces the three-dimensional problem to a two-dimensional one with a special symmetry.

It would be possible now to replace the set of equations by, say, a second-order finite difference equivalent. There are serious problems with this procedure since the stress boundary conditions require computation of derivatives which reduces the precision of the solution. Furthermore, we shall eventually be interested in computing far-field radiation which is actually proportional to slip velocity rather than slip at the fault. Precision would be reduced again when taking time differentials of the solution to compute slip velocity.

A more appropriate method is to transform the equations of motion into a system of first-order hyperbolic equations. The variables now are the three particle-velocity components and the six stresses. We get.

$$\rho \dot{u}_{,t} = 1/r(r\Sigma_{rr})_{,r} + 1/r(\Sigma_{r\phi} - \Sigma_{\phi\phi}) + \Sigma_{rz},_z$$

$$\rho \dot{v}_{,t} = 1/r(r\Sigma_{r\phi})_{,r} + 1/r(\Sigma_{r\phi} - \Sigma_{\phi\phi}) + \Sigma_{z\phi},_z$$

$$\rho \dot{w}_{,t} = 1/r(r\Sigma_{zr})_{,r} + 1/r\Sigma_{z\phi} + \Sigma_{zz},_z$$

$$\Sigma_{rr},_t = (\lambda + 2\mu)\dot{u}_{,r} + \lambda/r(\dot{u} + \dot{v}) + \lambda \dot{w}_{,z}$$

$$\Sigma_{zz},_t = \lambda \dot{u}_{,r} + \lambda/r(\dot{u} + \dot{v}) + (\lambda + 2\mu)\dot{w}_{,z}$$

$$\Sigma_{\phi\phi},_t = \lambda \dot{u}_{,r} + (\lambda + 2\mu)(\dot{u} + \dot{v})/r + \lambda \dot{w}_{,z}$$

$$\Sigma_{r\phi},_t = \mu \dot{v}_{,r} - \mu(\dot{u} + \dot{v})/r$$

$$\Sigma_{z\phi},_t = \mu \dot{v}_{,z} - \mu \dot{w}/r$$

$$\Sigma_{zr},_t = \mu \dot{w}_{,r} + \mu \dot{u}_{,z} \qquad\qquad (9)$$

where the commas indicate a partial derivative with respect to the subscripted variable following the comma. Dots indicate time derivatives; i.e., $\dot{u}$, $\dot{v}$, $\dot{w}$ are the components of

particle velocity. $\Sigma_{rr}, \Sigma_{\phi\phi}, \Sigma_{zz}$ and Σ_{zr} are functions of (r, z) related to the stresses by $\sigma_{rr} = \Sigma_{rr} \cos \phi$, etc. $\Sigma_{r\phi}$ and $\Sigma_{z\phi}$, on the other hand, are related to $\sigma_{r\phi}$ and $\sigma_{z\phi}$ by $\sigma_{z\phi} = \Sigma_{z\phi} \sin \phi$, etc. We have to solve (9) subject to the following boundary conditions on $z = 0$

$$\Sigma_{rz} = -\Sigma_{\phi z} = -\tau_e \qquad\qquad r < \min(v_R t, a)$$

$$\dot{u} = \dot{v} = 0 \qquad\qquad r > \min(v_R t, a) \quad (10)$$

and

$$\Sigma_{zz} = 0 \qquad\qquad \text{for all } r.$$

These boundary conditions can be used directly in the solution of the problem without differentiation.

So far we purposely avoided the problem of frictional arrest of sliding. We shall assume that slip at any point on the fault is arrested when the slip velocity $\Delta \dot{u}_x = 0$. $\Delta \dot{u}_x$ can be written in terms of the $\dot{u}$ and $\dot{v}$ functions defined in (8) as

$$\Delta \dot{u}_x = 2\dot{u} \cos^2 \phi - 2\dot{v} \sin^2 \phi$$

$$\Delta \dot{u}_y = (\dot{u} + \dot{v}) \sin 2\phi.$$

As we mentioned before $\Delta \dot{u}_y$ was found to be practically equal to zero ($\psi \approx 0$) within the accuracy of our numerical scheme in all the cases we studied. The condition $\Delta \dot{u}_y = 0$ is equivalent to $\dot{u} = -\dot{v}$ so that

$$\Delta \dot{u}_x = 2\dot{u} = -2\dot{v} \qquad\qquad\qquad (11)$$

which illustrates the interesting result that $\Delta \dot{u}_x(r, t)$ is not a function of the longitude ϕ on the fault. Slip arrest preserved the symmetry of the problem so that we can change the stress boundary condition on the fault to $\dot{u} = \dot{v} = 0$ after healing.

There is little hope of obtaining analytical solutions to the problems we have posed. A solution was obtained by Kostrov (1964) for the self-similar circular shear crack (see equation 14), and the near-field displacements have been computed by Richards (1973) for elliptical and circular faults using a Cagniard-de Hoop technique. For cracks that stop, the problem has a characteristic length and the solution is not a homogeneous function of space and time as in the self-similar problem. The solution in this case leads to a problem of multiple diffractions at the edges of the fault. Even if we could solve these multiple diffractions, we would have to compute series of multiple singular integrals in space and time. As discussed by Kostrov (1974b) for the plane problem, it would be more economical to start with a numerical method from the outset. We have solved the circular fault models studied in this paper using the finite difference method described in the appendix. It is an explicit leap-frog method in a grid staggered both in space and time. This grid was specifically designed to minimize the instabilities produced by the singularities at the edges of the fault. The numerical method has been extensively tested against the self-similar solution (Kostrov, 1964), the static slip when friction does not stop sliding (Keilis-Borok, 1959), and the dynamics of the diffracted wave fronts.

SOLUTION FOR THE SLIP AT THE FAULT

Scaling. A dimensional analysis of the system (9) permits the representation of solutions in terms of non-dimensional variables. This is very convenient because it makes explicit the dependence of the solution on the source parameters. We have chosen the following

scaling

Length	$r = ar'$	
Time	$t = a/\alpha t'$	
Stress	$\sigma_{ij} = \tau_e \sigma'_{ij}$	
Displacement	$u_i = \tau_e/\mu a u_i'$	
Seismic moment	$M_o = \tau_e a^3 M_o'$	
Energy	$E = \tau_e^2/\mu a^2 E'$.	(12)

where non-dimensional variables are indicated by a prime. The physical variables are: a, the final source radius, τ_e, the effective stress; α, the P-wave velocity, and μ, the rigidity. We shall assume that $v = 0.25$ so that $\lambda = \mu$ and $\alpha = \beta\sqrt{3}$. The scaling of any
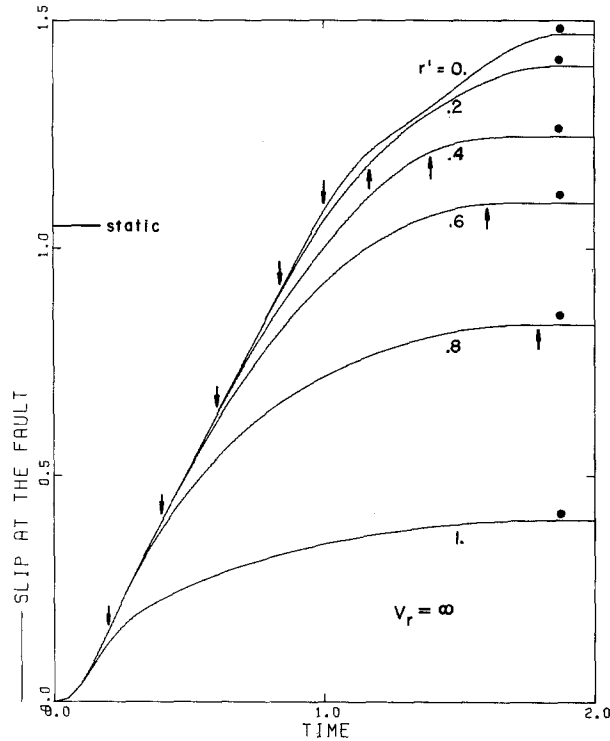

Fig. 2. Source slip function for the instantaneously appearing circular fault. The slip is shown at several radial distances from the origin. The slip at $r' = 1$ is not zero because the actual fault length is slightly larger than 1 as a consequence of the discretization. The down-pointing arrows indicate the arrival of the first stopping phase at $r' = 0.8$, etc. while the up-pointing arrows indicate the arrival of the stopping phase from the farthest point on the edge of the fault. The circles indicate the points at which slip is arrested by friction. The static line indicates the slip at the center ($r' = 0$) in the static solution. The dynamic overshoot is clear in this figure.

other variable may be deduced from (12). We have chosen α as the unit of velocity, instead of the shear-velocity, because it is more convenient in the numerical method.

The instantaneous circular fault. We shall study this problem mainly because of its simplicity, although it cannot be realized because it violates causality. It is well known that the maximum rupture velocity for real cracks is the Rayleigh-wave velocity or the P-wave velocity for cracks without cohesion (Burridge and Levy, 1974). The problem is also interesting because it appears to be closely related to the widely used model whose radiation was approximated by Brune (1970). In Figure 2 we present the source slip

function Δu_x at several radial positions on the fault. The slip has been computed integrating numerically the slip velocity $\Delta \dot{u}_x$ defined in (11). Some smoothing due to the numerical method is clearly present at $t = 0$, but no spurious oscillations due to numerical dispersion are apparent. Immediately after rupture, the slip increases linearly with time, that is, with constant slip velocity. This slip velocity is $\Delta \dot{u}_x' = 2/\sqrt{3}$ (or $\Delta \dot{u}_x = 2\beta\tau_e/\mu$) as predicted by Brune (1970). Slip decreases after the arrival of the waves radiated from the edges of the fault. The first arrow in Figure 2 marks the arrival time of the P wave radiated from the nearest point on the edge, while the second one indicates the P wave from the farthest point on the edge.

Slip at a point on the fault stops when the slip velocity tends to reverse its sign. If the point tried to slip back, the frictional resistance (2) would reverse its sign blocking any further slip. Once a point is blocked it will not slip until the stress overcomes the static friction again. As the circles in Figure 2 indicate, all the points on the fault get blocked at the same time so that the whole fault gets healed instantaneously. The final slip (after the fault is healed) is

$$\Delta u_x = \tau_e/\mu a D(1 - r^2/a^2)^{1/2} \tag{13}$$

within the precision of our numerical solution. This is of the same form as the slip in the well-known static solution of Keilis-Borok (1959). However, the slip at the center, $D = 1.52$, is larger by a factor of about 1.34 than the value expected from the static solution. This dynamic overshoot is a usual occurrence in relaxation problems.

After the fault is healed, the boundary conditions (10a) on the fault change to $\dot{u} = \dot{v} = 0$ and the calculation of stresses and velocities may proceed with the same numerical method. Alternatively, we can use a representation theorem since we know now the complete history of slip at the fault. This is the method we shall use to compute far-field radiation.

As a consequence of the dynamic overshoot of slip, the final static stress drop $\Delta\sigma$ on the fault is larger than the effective stress τ_e. In fact, because of the particular form of the final slip (13), the stress drop $\Delta\sigma = 1.34 \, \tau_e$ at any point on the fault. Thus, the final stress on the fault τ^f is lower than the frictional stress τ^k.

The subsonic circular fault. Let us consider now the more realistic problem of a circular fault that grows at a constant subsonic velocity until it suddenly stops expanding. The process by which rupture stops is certainly quite artificial but it is required to preserve the cylindrical symmetry. A constant rupture velocity was adopted in order to study the effect of this parameter on the dynamics of the fault. Variable velocity can be easily introduced in the numerical solution so long as the circular fault shape is maintained. The use of variable velocity is probably not justifiable unless we compute the rupture velocity from a given distribution of fracture energy on the fault. Such a problem is beyond the scope of the present study.

We computed the slip function at the source for several rupture velocities between $v_R' = 0.35$ ($v_R = 0.6\beta$) and $v_R' = 0.52$ ($v_R = 0.9\beta$). This range appears to cover the probable values of average rupture velocity of earthquake faults and experimental models. In Figure 3 which shows a three-dimensional plot of the fault slip function $\Delta u_x'$ (x', t') for $v_R' = 0.43$ ($v_R = 0.75\beta$). This source function is surprisingly simple and quite similar to those found by Burridge (1969) for similar problems of plane faults. The initial part of the source function, before the arrival of the P "stopping" phase, is the same as the solution obtained by Kostrov (1964) for a self-similar circular shear fault

$$\Delta u_x' = A_o \sqrt{t'^2 - r'^2/v_R'^2} \qquad \text{for } t' > r'/v_R' \tag{14}$$

where A_o is the constant slip velocity at the center of the fault. This constant can be

easily derived from the constant $C = A_0 \times \alpha/\beta$ computed by Dahlen (1974). A_0 varies from 0.57 at $v_R = 0.6\beta$ to 0.81 at $v_R = 0.9\beta$.

In Figure 4 we show the source slip functions at several values of the radius r'; in this case $v_R' = 0.52$ ($v_R = 0.9\beta$). In the same figure we indicate with dashed lines the exact
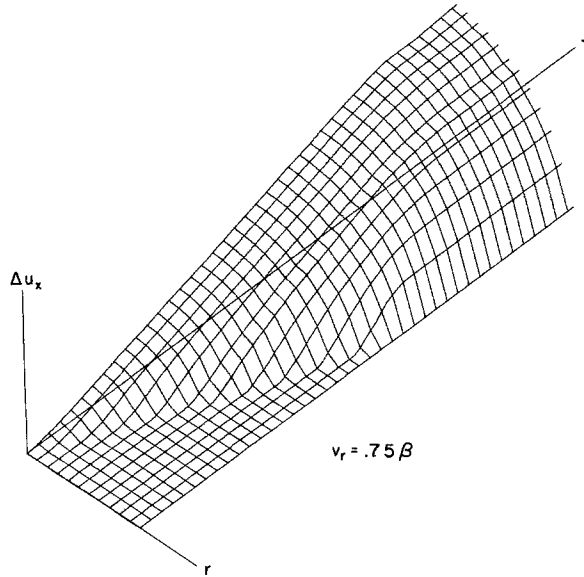

FIG. 3. Source slip function for a subsonic circular fault with $v_R = 0.75\beta$. This is a composite plot of the slip history as a function of radius on the fault.
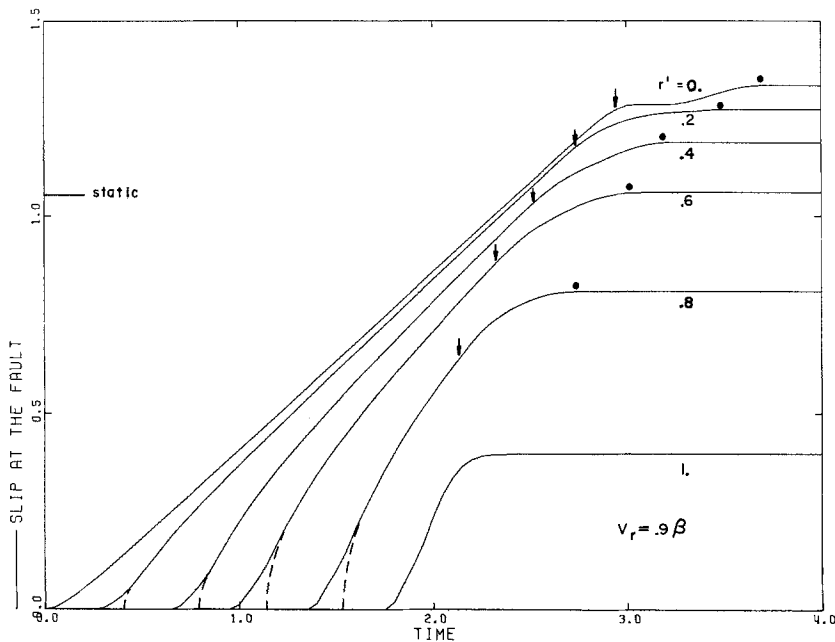

FIG. 4. Source slip function for a subsonic fault with $v_R = 0.9\beta$. This figure illustrates the concentration of slip at the center of the fault. The arrows indicate the arrival of the stopping phases. The circles indicate the time of slip arrest at the fault. As in Figure 2, the line marked static indicates the static solution at $r' = 0$.

solution (14) where it differs significantly from the numerical solution. The difference is important only near the rupture front where the singular slip velocity implied by (14) is smoothed by the numerical scheme. In Figure 4 we indicate with arrows the arrival of the P stopping phase from the edge; this is the wave radiated when the rupture front suddenly stops. A dot indicates the point where slip arrest occurs. As opposed to the case of instantaneous rupture, slip does not stop simultaneously on the fault plane. It appears as if a "healing" wave propagates inward from the edge of the fault some time after the P and S stopping phases. The velocity of this healing wave appears to be variable, but it is difficult to calculate due to numerical uncertainty in determining the healing time. The "bump" in slip function for $r' = 0$ appears in the solution for all v_R"s we have studied.

The slip at the fault again overshoots the static solution as indicated in Figure 4 for the slip at the center of the fault. The overshoot depends on the rupture velocity and varies slightly from 15 per cent at $v_R = 0.6\beta$ to about 20 per cent at $v_R = 0.9\beta$. Due to the overshoot the static stress drop $\Delta\sigma$ will be larger than the effective stress. The relaxation from the effective stress to the final stress drop occurs after the fault is healed. In all the cases studied the final slip at the source differed very little from the elliptical distribution $\Delta u' = D \sqrt{1-r'^2}$ so that the stress drop $\Delta\sigma'$ is effectively constant over the fault. $\Delta\sigma'$ varies from 1.15 at $v_R = 0.6\beta$ to 1.2 at $v_R = 0.9\beta$.

FAR-FIELD BODY-WAVE RADIATION

Representation theorems. The body waves radiated from the fault can be computed directly from the slip-velocity function using the representation theorems (Burridge and Knopoff 1964). Referring to the coordinate system shown in Figure 1, we write the representation theorem in the form

$$u(\vec{R}, t) = \frac{1}{4\pi\rho c^3} R_{\theta\phi} \frac{1}{R} \mu \iint dS \, \Delta\dot{u}_x\left(r, \phi, t - \frac{R}{c} + \frac{\hat{R}\cdot\vec{r}}{c}\right) \tag{15}$$

where, $\vec{R}$ is the position vector of the observer, $R_{\theta\phi}$ is the P or S radiation pattern, r and ϕ are cylindrical coordinates on the fault plane and c is the velocity appropriate for P or S waves. One could compute the far-field radiation directly from (15) by numerical integration, but this is very difficult due to the singularities in $\Delta\dot{u}_x$. A more convenient method is to work in the frequency domain, since we are interested in the far-field spectra. The Fourier transform of (15) is

$$u(\vec{R}, \omega) = \frac{1}{4\pi\rho c^3} R_{\theta\phi} \frac{1}{R} \exp\left[-i\omega(R/c)\right]\mu \iint dS \, \Delta\dot{u}_x(r, \phi, \omega) \exp\left[i\omega(\vec{R}\cdot\vec{r}/c)\right]. \tag{16}$$

The form of (15) and (16) is interesting since the integral

$$M_o(\hat{R}, \omega) = \mu \iint rdr \, d\phi \, \Delta\dot{u}_x(r, \phi, \omega) \exp\left[i\omega(\vec{R}\cdot\vec{r}/c)\right] \tag{17}$$

can be defined as the seismic moment spectral density. When $\omega \to 0$, $M_o(\hat{R}, \omega) \to M_o$ the seismic moment defined by Aki (1966).

In the special case of the shear fault with circular symmetry we can simplify (17) since $\Delta\dot{u}_x (r, \omega)$ is independent of ϕ as shown in (11). Let us first re-write (17) in the form

$$M_o(\hat{R}, \omega) = \mu \int_0^a rdr \, \Delta\dot{u}_x(r, \omega) \int_{-\pi}^{\pi} \exp\left[i(\omega r/c) \sin\theta \cos(\phi - \phi_0)\right] d\phi \tag{18}$$

where we used

$$\hat{R}\cdot\vec{r} = r \sin\theta \cos(\phi - \phi_0).$$

The second integral is, except for a factor of 2π, the definition of a Bessel Function so that

$$M_o(\theta, \omega) = 2\mu \int_0^a r\,dr\,\Delta\dot{u}_x(r, \omega) J_o\left(r\,\frac{\omega}{c}\sin\theta\right), \tag{19}$$

where we have made explicit that M_o is only a function of the azimuth θ measured from the normal to the fault. We can invert (19) to obtain

$$M_o(\theta, t) = 2\mu \int_0^a r\,dr \int_{t-\xi}^{t+\xi} d\tau \frac{\Delta\dot{u}_x(r, \tau)}{\sqrt{\xi^2-(t-\tau)^2}}, \quad \xi = \frac{r}{c}\sin\theta \tag{20}$$

and the far-field displacement

$$U_{FF}(\vec{R}, t) = \frac{1}{4\pi\rho c^3} R_{\theta\phi} \frac{1}{R} M_o(\theta, t-R/c). \tag{21}$$

Thus $M_o(\theta, t)/\mu$ contains all the time-dependence of the far-field seismogram, and we shall refer to it as the far-field pulse.

We can extract information about the far-field spectrum $M_o(\theta, \omega)$ analyzing (19) in some detail. We recognize the integral on the right of (19) as the Hankel transform of $\Delta\dot{u}(r, \omega)$ in the radial variable. Designating this transform with a tilde

$$M_o(\theta, \omega) = 2\pi\mu\widetilde{\Delta\dot{u}}_x(k, \omega)\big|_{k=\omega/c\sin\theta}. \tag{22}$$

A relationship similar to this was found by Aki (1967) for long, thin faults (finite line source). A physical interpretation of (22) follows from the observation that $c/\sin\theta$ is the phase velocity along the fault of a cylindrical wave radiated in the direction of the azimuth θ. Thus, $M_o(\theta, \omega)$ is the amplitude of this cylindrical wave and $\widetilde{\Delta\dot{u}}_x$ acts as the excitation function of these waves. The effect of the Hankel transform in (22) is to add a fractional high-frequency decay $\omega^{-1/2}$ to the far-field spectrum. These fractional decays have already been found by Savage (1974) in kinematic models and will be evident in our solutions. The most important consequence of (22) is that corner frequencies in the spectrum should result both from the finite rise time of the source function (ω transform) and from the finite radius of the fault (k transform). Corner frequencies appear in the spectrum whenever the original function has a finite duration. In the specific example of a circular fault, the rise time is approximately of the order of $2a/\beta$ so that both corner frequencies are of similar magnitude. This is a unique property of circular faults since in elongated faults the rise time is controlled by the narrower dimension.

We computed the far-field spectra from the Fourier-Hankel transform of the source slip-velocity function (22). Since we had a numerical solution for $\Delta\dot{u}_x$, we obtained the time transform by a numerical F.F.T. and the Hankel transform was computed by a numerical integration of (19). The far-field pulses were computed inverting $M_o(\theta, \omega)$ numerically with an F.F.T. program. This procedure is much more precise than a numerical evaluation of the singular integrals (20).

Radiation from the instantaneous circular fault. The far-field spectra of the body waves radiated from the instantaneously appearing fault are shown in Figure 5 for three values of the azimuth ($\theta = 0°, 45°$ and $90°$). The associated far-field pulses are shown in Figure 6. The far-field radiation varies significantly as a function of azimuth. The most significant difference is between radiation at nearly normal directions ($\theta \approx 0°$) and radiation at higher azimuths. This difference can be explained referring to (22) since when $\theta \approx 0°$, the Bessel function is approximately equal to one. The far-field displacement is then the

radial average of the slip-velocity function. Waves leave the source in phase so that there is no interference due to the finiteness of the fault. The spectrum at $\theta = 0°$ decays at high frequency like ω^{-1}, this decay being associated with the discontinuity of the pulse at $t = 0$. This step-like behavior is due to the sudden jump in slip velocity when the fault appears instantaneously.

For azimuths $\theta \gtrsim 30°$ the waves leave the source at an angle and interference effects appear in the spectrum. The spectra and pulses change very slowly with azimuth in this range. At high frequencies, the spectrum of P and S waves decays like $\omega^{-5/2}$. As is well
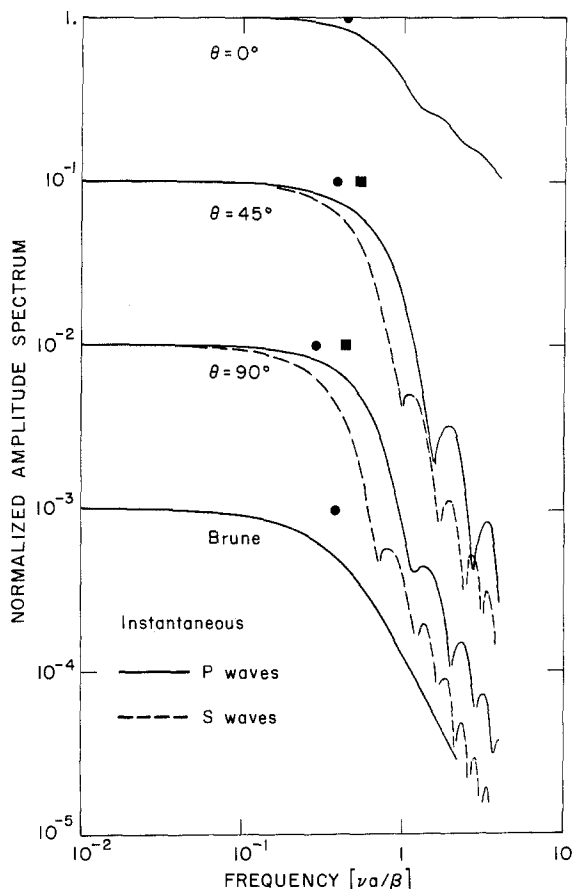

FIG. 5. Far-field spectrum of P and S waves radiated by an instantaneous circular fault. The spectra, shown for three azimuths $\theta = 0°$, $45°$ and $90°$, are shifted by one decade in amplitude for purposes of clarity. The squares indicate the P corner frequency while the circles indicate the corner-frequency of S waves. For comparison we include the spectrum of S waves proposed by Brune (1970).

known from Fourier transform theory, this decay is associated with the dominant singularity in the time pulse. The $\omega^{-5/2}$ decay corresponds to a singularity of the type $(t-t_0)^{3/2} H(t-t_0)$. This is precisely the behavior near the wave front of the far-field pulses at $\theta = 45°$ and $90°$ shown in Figure 6; the $\delta t^{3/2}$ behavior is associated with the waves radiated from the edge of the fault at the time of the sudden rupture on the fault. As indicated in (21), we measure time with respect to the arrival from the center of the fault. Thus, the first arrival comes from the point on the edge of the fault which is closer to the observer with a time advance $-a \sin \theta/c$. This theoretical time is indicated by the first arrow in the far-field pulses of Figure 6.

Another important feature of the far-field spectra are the "holes" at high frequencies. The frequency of holes is given approximately by multiples of $v = c/(2\,a_e \sin \theta)$, where $a_e = 0.73a$ is a sort of effective radius. It is smaller than real radius because of the concentration of slip and rise time near the center of the fault. Points near the center of the fault radiate more "intensely" than those near the fault edge. We can also relate the holes in the spectrum to the width of the far-field pulse. In the far-field pulses of Figure 6 we indicate with the second arrow the theoretical arrival time of the radiation from the farthest point on the edge of the fault. The time delay for this arrival is $a/c \sin \theta$. The
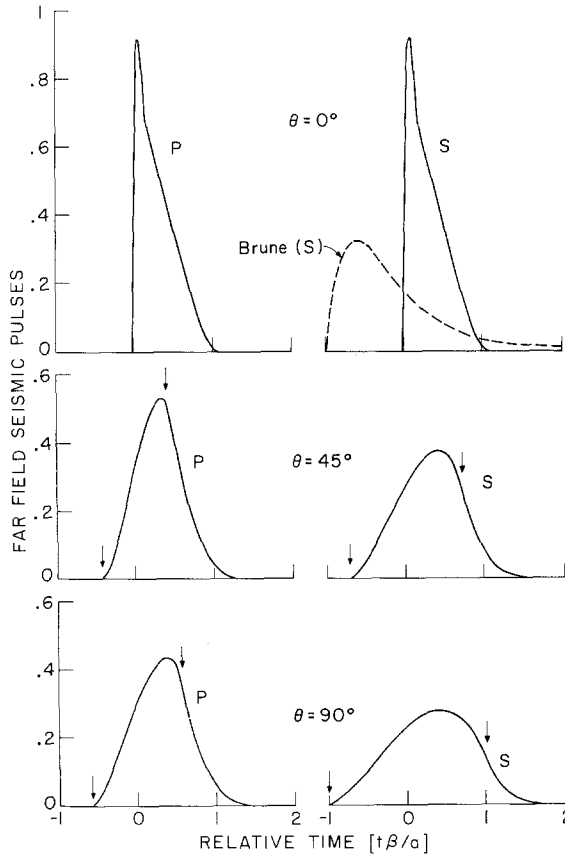

FIG. 6. Far-field seismic pulses radiated by an instantaneous circular fault. The displacement pulses are shown for $\theta = 0°$, $45°$ and $90°$. Time is measured relative to the arrival from the center of the fault. The arrows indicate the arrival time of waves radiated from the nearest and farthest point on the edge of the fault. The far-field pulse assumed by Brune (1970) is shown for comparison. The pulses are scaled by a constant time integral (low-frequency level).

interval $2a/c \sin \theta$ between the arrows is a good measure of the pulse width and is inversely proportional to the frequency of the first hole in the spectrum. For real faults, however, the holes will probably be "filled" with radiation due to inhomogeneities of the effective stress or to scattering by inhomogeneities.

The corner frequencies of the spectra in Figure 5 were determined by the intersection of the low- and intermediate-frequency trends of the spectrum. The corner frequencies are indicated with a circle for S waves and a square for P waves. A clear variation of the corner frequencies with azimuth is observed in these spectra. In Figure 7 we show the variation of the P and S corner frequencies as a function of azimuth. Near $\theta = 0°$ the

behavior is rather complicated because of the change in the asymptotic decay at high frequencies. For azimuths higher than about 30°, the corner frequency decreases systematically with increasing azimuth. This decrease of the corner frequency is matched by the widening of the far-field pulses observed in Figure 6. This is a clear indication that the corner frequencies, like the holes, are a measure of the width of the far-field seismic pulse. Since the pulse widths themselves are proportional to the fault size, the corner frequency should be also a measure of the size of the fault. The corner frequencies of P waves are higher than the corner frequency of S waves by a factor close to 1.5 in the range $\theta > 30°$. This result has a simple interpretation in terms of the width of the far-field pulse. The P pulses are clearly narrower than the S pulses, that
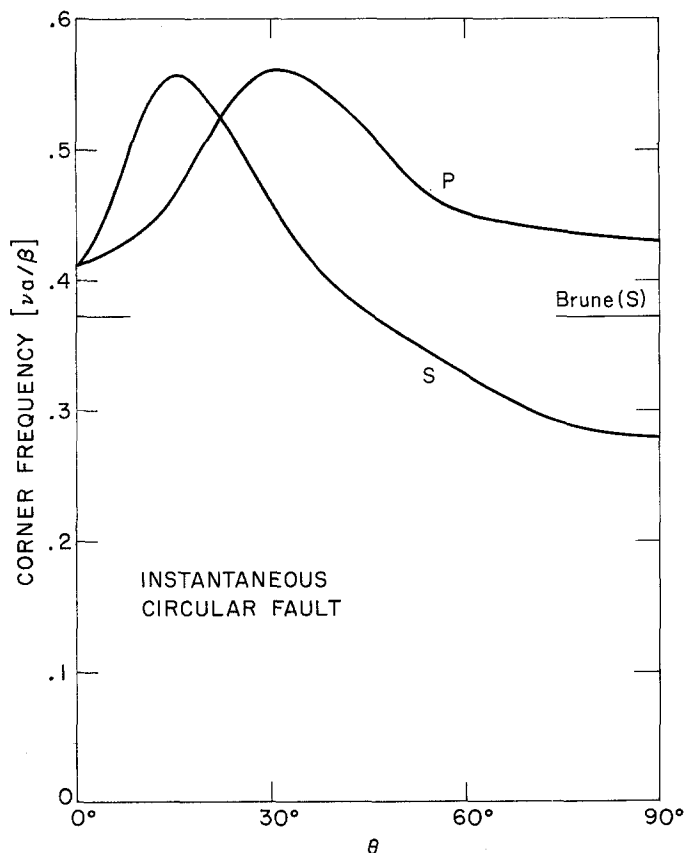

FIG. 7. Variation of corner frequencies as a function of azimuth for the instantaneous circular fault. Brune's approximation is included for comparison.

is there is more high-frequency content in P pulses than in the S pulses. The reason the P pulses are narrower than S pulses is that the arrivals from the closest and farthest points on the edges will be less separated in time due to the faster velocity of P waves.

As was mentioned in the previous section, Brune (1970) attempted to obtain the far-field radiation of S waves from a model that approximates an instantaneous circular fault. The spectrum and far-field pulse assumed by Brune (1970) are shown for comparison with our results in Figures 5 and 6. The relation between his pulse and the numerical solutions for S waves is rather poor except that the widths are similar. This is reflected in the spectra in Figure 5 since, although the high-frequency decay is different (ω^{-2} in Brune's and $\omega^{-2.5}$ in ours), the corner frequencies are not too different. Brune (1970)

assumed that the S waves were radiated normally to the fault and neglected the effect of the edges of the fault. This assumption means, of course, that the P waves are not accounted for and explains the wrong high-frequency decay. It is interesting that the corner frequency is still close to ours in spite of these differences.

Radiation from a subsonic circular fault. In Figures 8 and 9 we show the far-field pulses and their spectra radiated from a subsonic circular fault with a rupture velocity $v_R' = 0.52$ ($v_R = 0.9\beta$). We have computed the far-field radiation for several other rupture velocities in the range $(0.6\beta-0.9\beta)$. The general features of the results in Figures 8 and 9 were not
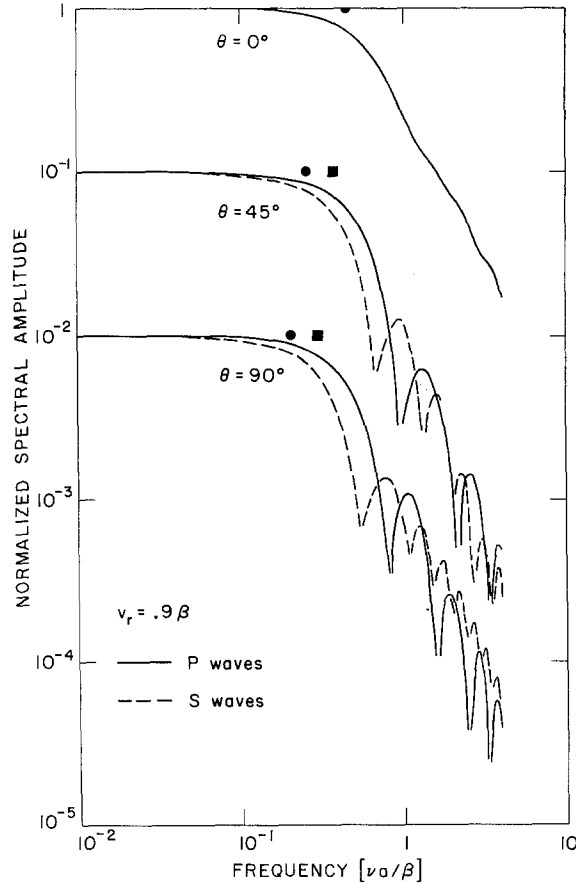

FIG. 8. Far-field spectrum of P and S waves radiated by a subsonic circular fault with $v_R = 0.9\beta$. The spectra for different θ are shifted by one decade in amplitude. The squares indicate the P corner frequencies while the circles indicate the S corner frequencies.

significantly affected by the variation of the rupture velocity. The spectra are much more complicated than those for the instantaneous fault; in fact, at least one intermediate frequency trend may be identified in most spectra. For large azimuths, $\theta > 30°$, we can clearly identify segments of the spectra that decay like ω^{-2} in both P and S waves. In the S spectra for $\theta > 45°$ we can also identify an $\omega^{-1.5}$ intermediate slope. These complicated variations of the spectrum cannot be easily related to the features of the time pulses. In fact, these pulses have the t^2 behavior near the wave front that was predicted by Dahlen (1974). This is the wave front radiated from the neighborhood of the nucleation point. Associated with this singularity there should have been an ω^{-3} high-frequency slope. The ω^{-2} or $\omega^{-1.5}$ slopes observed in our results are probably associated with the stopping

phases radiated when the fault stops expanding. In Figure 9 we indicate with arrows the geometrical arrival times of the stopping phases from the nearest and farthest points on the edge of the fault. The time delays of these stopping phases are

$$\Delta t = a\left(\frac{1}{v_R} \pm \frac{\sin\theta}{c}\right). \tag{23}$$

As observed in Figure 9, these stopping phases control the width of the far-field pulse. Without using a specific measure of the pulse width, we simply point out the obvious correlation: The corner frequencies in Figure 8 are higher or lower depending on the
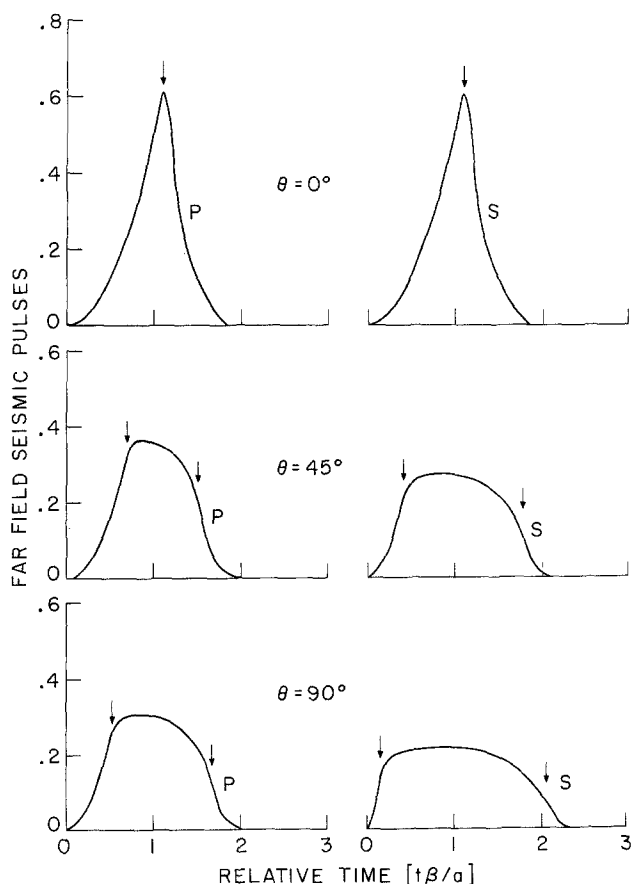

FIG. 9. Far-field displacement pulses radiated by a subsonic circular fault. Time is measured relative to the arrival from the nucleation point at the center of the fault. The arrows indicate the arrival time of stopping phases from the nearest and farthest points on the edge of the fault. The displacement pulses are scaled by a constant time integral (constant low-frequency level).

width of the pulse. Then, the intermediate slopes are intimately related to the variation of the corner frequencies. We can define three distinct regions in the far-field spectrum: First, the long-period or low-frequency region is controlled by the seismic moment of the fault; in this region the spectrum is flat since the fault appears as a point source. Second, the intermediate frequency region is controlled by the width of the pulse and, in a final analysis, by the size of the fault. This region is quite complicated and the envelope of the spectrum may have several decay rates depending on the azimuth of the observer. This region also controls the energy of the far-field radiation since the velocity spectrum has a

peak close to the corner frequency of the displacement spectrum. Finally, the high-frequency region is controlled by the discontinuities of the seismic pulse. In actual observations, this region will probably be obscured by radiation from irregularities in the fault. Dahlen's (1974) high-frequency slope pertains to this region; this explains why he found corner frequencies which are much higher than ours.

The complicated envelope of the spectrum makes it quite difficult to determine corner frequencies in a unique way. We have used the standard procedure of observational work, that is, we fitted a straight line to the intermediate frequency region. The corner frequency
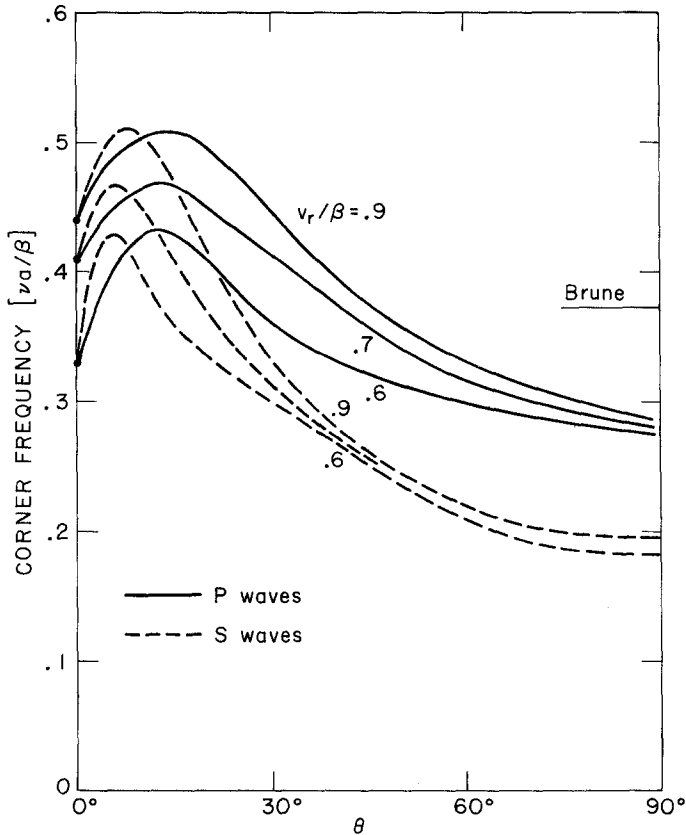

FIG. 10. Variation of P and S corner frequencies as a function of azimuth for three values of the rupture velocity.

is then determined as the intersection of this slope and the constant low-frequency asymptote. This method is subject to errors even for these numerical results; we consider that the precision of our corner frequencies is not better than 10 per cent. In Figure 8, the circle indicates the S corner frequency and the square, the P corner frequency. The variation of the corner frequencies with azimuth is shown explicitly in Figure 10 for $v_R = 0.9$, 0.75 and 0.6β. Like in the instantaneous fault, radiation in the cone $\theta < 30°$ is anomalous. This anomalous behavior is related to the change of intermediate frequency slope near $\theta = 0$. For $\theta > 30°$ the variation is slow and both corner frequencies decrease with θ.

The corner frequency of P waves is higher than the corner frequency of S waves for $\theta > 30°$. This relation between the corner frequencies reflected the longer duration of

the S pulses compared to the P pulses. This, in turn, is a consequence of the delay between the arrival of the two principal stopping phases. This ratio of the corner frequencies appears to be typical of circular or nearly circular faults and is opposite to that predicted for linear (elongated) faults by Savage (1972). As shown by Molnar *et al.* (1973), there is substantial evidence that in a great number of observations the P corner frequency is larger than the S corner frequency. The maximum ratio of about 1.5 predicted by our model is less than that reported by Molnar *et al.* (1973) for certain observations.

The corner frequencies of S waves in Figure 10 are significantly lower than the corner frequency proposed by Brune (1970). We have computed the following average values for the corner frequencies at $v_R/\beta = 0.9$.

$$v_0{}^{S'} \text{ (Hz)} = 0.21 \, \beta/a$$

$$v_0{}^{P} \text{ (Hz)} = 0.32 \, \beta/a \tag{24}$$

where $v_0{}^{S}$ and $v_0{}^{P}$ are the corner frequencies. Our average $v_0{}^{S}$ is about a factor of two lower than Brune's $v_0{}^{S} = 0.375 \, \beta/a$.

The stress drops are usually determined from observations of v_0 and M_o. The seismic moment M_o, computed from (17) is

$$M_o = \mu \overline{\Delta u_x} \pi a^2 = 16/7 \Delta \sigma a^3. \tag{25}$$

Using the corner frequency-versus-radius relation (24) we would obtain stress drops which are about eight times those found using Brune's approximation.

TOTAL SEISMIC ENERGY RADIATION AND EFFICIENCY

The total seismic energy E_s radiated from a general fault was determined by Kostrov (1974a) as

$$E_s = 1/2 \int_\Sigma (\sigma_{ij}^0 - \sigma_{ij}^f) \Delta u_i{}^f n_j \, dS + \int_0^{t_m} dt \int_{\Sigma(t)} \Delta u_i (\partial/\partial t) \sigma_{ij} n_j \, dS - E_f \tag{26}$$

where σ_{ij}^0 is the initial stress, σ_{ij}^f is the final static stress, $\Delta u_i{}^f$ is the final slip at the fault, $\Sigma(t)$ is the fault area at time t, while Σ is the final source area, n_j is the normal to the fault, and t_m is the time to reach the static equilibrium. We can simplify this equation because of the circular symmetry of our faults

$$E_s = \pi \int_0^a r dr (\sigma_{zx}^0 - \sigma_{zx}^f) \Delta u_x{}^f + 2\pi \int_0^{t_m} dt \int_0^a r dr \Delta u_x (\partial/\partial t) \sigma_{zx} - E_f. \tag{27}$$

The E_f term in (26) or (27) is the total energy absorbed at the edge of the fault while it expands subsonically. This energy may be written as

$$E_f = \int_0^{t_m} dt \, v_R t \int_0^{2\pi} d\phi \, v_R G(v_R, t, \phi) \tag{28}$$

where $G(v_R, t, \phi)$, usually called energy release rate (Freund, 1972b), is the energy absorbed at the fault edge per unit length of the edge and per unit advance of the rupture front. This is the energy available for fracture and should be exactly equal to γ_S, the surface energy or fracture energy of the material. In the problems we have studied, the growth of the fracture surface is prespecified so that γ_S should be computed from the solution. In fact γ_S should be a given material property and the growth of the rupture front deduced from it (Kostrov, 1974a). Since we are studying models where the initial rupture is subsonic and self-similar, we can obtain E_f from Kostrov's (1964) solution for the self-similar circular shear crack. We get

$$E_f = \frac{\tau_e{}^2}{\mu} a^3 \, \pi/3 \, g(v_R) \tag{29}$$

where

$$g(v_R) = \pi/8 \ A_0{}^2 \ \alpha^2/v_R{}^2 \left(\frac{R(v_R)}{v_\beta} \frac{\beta^2}{v_R{}^2} + v_\beta \right),$$

$$R(v_R) = 4 v_\alpha v_\beta - (2 - v_R{}^2/\beta^2)^{1/2}$$

and

$$v_\alpha = \sqrt{1 - v_R{}^2/\alpha^2} \qquad v_\beta = \sqrt{1 - v_R{}^2/\beta^2}.$$

A_0 is the slip velocity at the center, defined in (14). We have computed $g(v_R)$ and found that it varies monotonically from 0.72 at $v_R = 0.6\beta$ to 0.54 at $v_R = 0.75\beta$ and 0.21 at $v_R = 0.9\beta$.

Let us consider now the second integral in (27); the argument of this integral contains the time derivative of the stress at the fault. During the slip process at the fault the stress is constant, $\sigma_{zx} = \tau^k$ so that there is no contribution to the integral during this time. As we discussed in the section, "Reduction to a Two-Dimensional Problem", there is a stress relaxation after the fault is locked due to the overshoot of the dynamic slip at the fault. During this relaxation, the slip remains fixed at $\Delta u_x{}^f$ and the source area $\Sigma(t) = \Sigma$ does not change. We can interchange the order of integrations in (27) to obtain

$$E_s = \pi \int_0^a r dr \, (\sigma_{xz}^0 - \sigma_{xz}^f) \Delta u_x{}^f + 2\pi \int_0^a r dr \, (\sigma_{xz}^f - \sigma_{xz}^k) \Delta u_x{}^f - E_f$$

$$E_s = \pi \int_0^a r dr \, (\sigma_{xz}^0 + \sigma_{xz}^f) \Delta u_x{}^f - 2\pi \int_0^a r dr \, \sigma_{xz}^k \Delta u_x{}^f - E_f. \tag{30}$$

The interpretation of this equation is interesting. The first integral is the decrease of strain energy due to faulting, while the second integral is the energy dissipated by friction.

The strain energy is partitioned into seismic energy, fracture energy, and frictional dissipation by the fault process. These processes are irreversible since the last two terms are dissipative so long as the rupture velocity is less than the Rayleigh velocity.

Since $\sigma_{xz}^0 = \tau^0$ and $\sigma_{xz}^k = \tau^k$ were defined to be constant and σ_{xz}^f was shown to be constant (within the precision of our solutions), we can simplify (30) to find

$$E_s = 1/2 \ \pi a^2 [\tau^0 + \tau^f - 2\tau^k] \overline{\Delta u_x}{}^f - E_f \tag{31}$$

where $\overline{\Delta u_x}{}^f$ is the average slip on the fault. Since, very approximately

$$\overline{\Delta u_x}{}^f = \frac{\tau_e}{\mu} a \, D \sqrt{1 - r^2/a^2}$$

(see the section "Reduction to a Two-Dimensional Problem") we get

$$\overline{\Delta u_x}{}^f = 2/3 \ D \frac{\tau_e}{\mu} a$$

and,

$$E_s = \frac{\tau_e{}^2}{\mu} a^3 \frac{\pi}{3} \{ D[2 - \Delta\sigma'] - g(v_R) \} \tag{32}$$

where $\Delta\sigma' = \Delta\sigma/\tau_e$ is the non-dimensional stress drop. If $\Delta\sigma' = 1$ and $g(v_R) = 0$, this relation would reduce to the more familiar form

$$E_s = \tau_e \overline{\Delta u} \ \pi a^2. \tag{33}$$

We can now find the seismic efficiency from its definition

$$\eta = E_s/W \tag{34}$$

where

$$W = \bar{\sigma} \,\overline{\Delta u}\, \pi a^2$$

is the strain energy release. Inserting E_s and W into (34) we find

$$\eta = \frac{1}{2}\frac{\tau_e}{\bar{\sigma}}\{2-\Delta\sigma'-g(v_R)/D\}. \tag{35}$$

The term in brackets is always less than one but the factor $\tau_e/\bar{\sigma}$ is inaccessible to seismic observations because $\bar{\sigma}$ depends on the absolute value of stress.

We can find now the apparent stress $\eta\bar{\sigma}$

$$\eta\bar{\sigma} = 1/2\,\tau_e\{2-\Delta\sigma'-g(v_R)/D\} \tag{36}$$

then the apparent stress is not a measure of the absolute stress as it has been assumed sometimes but is only another form of the effective stress. The effective stress in (36) satisfies the inequality $\eta\bar{\sigma} < \Delta\sigma/2$ derived by Savage and Wood (1971) from general considerations about relaxation processes. The apparent stress $\eta\bar{\sigma}$ has been determined from $\eta\bar{\sigma} = \mu E_s/M_o$ for many earthquakes (Aki, 1972; Thatcher and Hanks, 1973; Wyss and Molnar, 1972) for which the stress drop was also determined. In many of these observations the inequality was not satisfied. It is not clear whether this discrepancy with the theory is real or is a consequence of an overestimate of E_s by the energy-magnitude relation (as suggested by Wyss and Molnar (1972)).

COMPARISON WITH KINEMATIC MODELS

Kinematic models of the source slip function have been extensively used by seismologists to analyze seismic radiation. In kinematic models the source slip is specified on the basis of some plausible physical considerations rather than as a result of the stress relaxation process. The best known of these models is Haskell's (1964) model of a linear fault. This model is a valid approximation to the dynamic solution for a very thin fault, if the slip is determined from a two-dimensional static crack with a length equal to the fault width. This solution is valid down to wavelengths of the order of the fault width. The corner frequencies of this problem are determined only by the length of the fault (Savage, 1972) and are insensitive to the width or the rise time. The corner frequencies are a function of the azimuth with respect to the rupture direction rather than the azimuth with respect to the normal to the fault. Furthermore, corner frequencies of P waves are lower than those of S waves while the opposite is true in the circular fault. Thus, the radiation from this model differs significantly from the radiation from circular faults.

More closely related to the problem studied here is the circular kinematical model studied by Savage (1967, 1974); he assumed a circular slip front advancing at a constant rupture velocity so that the geometry is very similar to the model we have studied. Savage studied two models of the source time function. In the first he assumed that

$$\Delta u_x(r, t) = U(t-r/v_R)H(t-r/v_R). \qquad\qquad r < a. \tag{37}$$

This slip function differs from the dynamic solution in Figures 3 and 4 principally because of the assumption of constant source slip function. Slip in the dynamic solution is variable over the fault and the rise time is also variable. The center of the fault slips longer and more than points closer to the tip; the fault is "stiffer" near the tips than at the

center. Savage studied another model where the slip was weighted by an ellipsoidal function

$$\Delta u_x(r,\ t)\ =\ \sqrt{1-r^2/a^2}\,U(t-r/v_R)H(t-r/v_R) \qquad r < a. \quad (38)$$

This is a better approximation to the dynamic solution but it still fails to approximate the variable rise time of the dynamical model. Since the dislocation models were proposed in order to parameterize the far-field radiation, we may compare the far-field pulses and spectra in Figures 8 and 9 with those published by Savage (1966, 1974). The time signals look much smoother in our solutions than in the kinematical models but both are similar in shape. The spectra differ significantly in the high-frequency region. In Figure 11, we
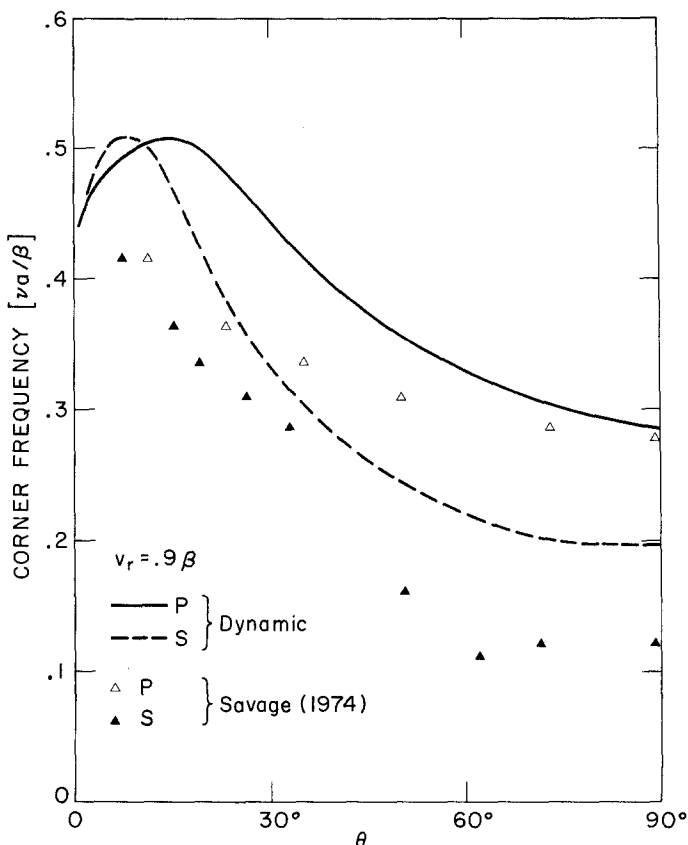

FIG. 11. A comparison of the corner frequencies of the far-field spectra from a dynamic circular fault with those of the kinematic circular fault (Savage, 1974); the rupture velocity $v_R = 0.9\beta$.

plot Savage's (1974) corner frequencies for model (37) and those obtained here. We have assumed $v_R = 0.9\beta$ in both cases. The range of the corner frequencies is similar in both cases although Savage predicted a wider range of variation. For azimuth $\theta > 30°$, the kinematic corner frequencies may be as low as one-half those for the dynamic model. This is a result of the wider far-field pulses in Savage's model.

DISCUSSION AND CONCLUSION

The model we have studied, a circular fault that grows at a constant velocity and stops suddenly, is certainly quite simple. Much of this simplicity is a result of the necessity

of preserving cylindrical symmetry in order to reduce the problem to a two-dimensional one. As a model of earthquake faulting in the Earth, this is an extremely simplified version of actual occurrence. In real faults, for instance, the effective stress is most probably variable due to both tectonic stress variations and frictional inhomogeneities. In our opinion, the assumption that has the most serious effects on the far-field radiation is that of circular symmetry of the final fault. Relaxation of this condition would require the use of the full three-dimensional numerical methods. The development of these methods is restricted by the large computer storage that would be required.

The effect of geometry may be visualized by comparison with the long thin fault model of Haskell (1964). In the latter case there are two very different length-scales, such that the corner frequency is determined by the length, while the rise time and the slip depend on the width of the fault. In the circular problem, the two scales coalesce and the rise time, slip, and corner frequencies are proportional to a single length-scale, the radius of the fault. In order to invert the corner frequencies to find the source dimensions, we would have to determine the geometry of the fault first, for instance, from surface data, aftershock observations, corner frequency ratios, etc. For geometries other than these two extremes there are no dynamic solutions available so that the transition between them is unknown.

The source slip functions that we obtain are quite different from the constant source functions usually assumed in kinematic models. In a circular fault, the slip is larger and the rise time is longer at the center of the fault. A consequence of this variation is that the fault has an effective radius which is smaller than the physical radius of the source. In all of the problems we studied, the fault overshoots the expected static slip so that the stress drop is larger than the effective stress. A consequence of this larger stress drop is that the apparent stress is proportional to the effective stress by a factor which is less than one-half. This relation reflects the fact that the dynamic elastic field created by a fault is sensitive only to changes of stress at the fault, but has no information about the absolute state of stress at the fault. This is a natural consequence of the linearity of the problem. The information about the absolute stress level is present only on the dissipative processes at the fault.

The far-field radiation from the fault was studied in detail. We identified three regions in the far-field spectrum: first, the usual constant low-frequency level; second, the intermediate frequencies, related to the fault size, which are the most complicated, because in this region the radiated waves are in near-resonance with the fault. The study of this region requires the use of full-wave methods like the numerical methods we have used. Finally, in the high-frequency range, the spectrum may be studied with the use of geometrical optics since the spectral density is determined by the dynamics of the wave fronts radiated from the edge of the fault.

The corner frequency is inversely proportional to the width of the far-field pulses, which in turn are controlled by the time lag between the stopping phases radiated from the nearest and farthest points on the fault. These relations provide the physical justification for the inverse relation between corner frequency and radius. Additionally, the corner frequency of P waves are larger by factors of up to 1.5 than the S corner frequency for most points on the focal sphere. We expect that these relations remain true for non-elongated faults.

The corner frequencies that we find for the dynamical model are about a factor of one-half of those predicted by Brune's (1970) relationship. This implies corrections by a factor of two to the source radius, and by a factor of eight to the stress drops determined from this relationship. The rather large correction to the stress drop is a result of the high sensibility of stress-drop estimates not only to the observational error of the corner

frequencies but also to the model assumed. The problem is even more evident in the case of elongated faults where the inversion of the stress drop requires the estimation of both the width and length of the fault. The inversion of the stress drop from far-field observations is an involved problem that requires data from different azimuths and hopefully, additional information to help in establishing the geometry of the source.

ACKNOWLEDGMENTS

APPENDIX

The Finite Difference Method

We discuss a method for the numerical solution of the boundary value problem (9, 10). Let us first rewrite the equations of motion in terms of the non-dimensional variables defined by (12). In a compact matrix notation the equations are

$$\mathbf{V},_t = \mathbf{A}\,\boldsymbol{\Sigma},_r + \mathbf{B}\,\boldsymbol{\Sigma},_z + 1/r\,\mathbf{C}\,\boldsymbol{\Sigma}$$

and

$$\boldsymbol{\Sigma},_t = \mathbf{D}\mathbf{V},_r + \mathbf{F}\mathbf{V},_z + 1/r\,\mathbf{G}\mathbf{V}$$ (A1)

where

$$\mathbf{V}^T = [\dot{u}', \dot{v}', \dot{w}']$$

and

$$\boldsymbol{\Sigma}^T = [\Sigma_{rr}, \Sigma_{zz}, \Sigma_{\phi\phi}, \Sigma_{r\phi}, \Sigma_{z\phi}, \Sigma_{zr}]$$

The matrices $\mathbf{A}, \mathbf{B}, \mathbf{C}, \mathbf{D}, \mathbf{F}$ and $\mathbf{G}$ are very sparse constant matrices whose only coefficients different from zero are

$$a_{11} = a_{24} = a_{36} = 1/3$$

$$b_{16} = b_{25} = b_{32} = 1/3$$

$$c_{11} = -c_{13} = c_{14} = -c_{23} = c_{35} = c_{36} = 1/3$$

$$c_{24} = 2/3$$

$$d_{11} = 3, d_{21} = d_{31} = d_{42} = d_{63} = 1$$

$$f_{23} = 3, f_{13} = f_{33} = f_{52} = f_{61} = 1$$

$$g_{31} = g_{32} = 3, g_{11} = g_{12} = g_{21} = g_{22} = -g_{41} = g_{42} = -g_{53} = 1.$$

The boundary conditions (10) on $z' = 0$ are

$$\Sigma_4 = -\Sigma_5 = 1 \qquad\qquad r' < \min(v_R't', 1)$$

$$v_1 = v_2 = 0 \qquad\qquad r' > \min(v_R't', 1)$$

$$\Sigma_2 = 0. \qquad\qquad\qquad\qquad\qquad\qquad (A2)$$

The system of equations in (A1) is a first-order hyperbolic system (Rychtmyer and Morton, 1957). Appropriate finite difference methods to solve these systems are of leap-frog type. The separation of time and space derivatives of the same variable in (A1) suggests the use of a staggered grid in time. In the staggered grid we define the velocities $\mathbf{v}$ at times $k\Delta t$ and the stresses Σ at times $(k+1/2)\Delta t$ where Δt is the time grid interval. The space grid may also be staggered in many different forms. We have adopted the grid shown in Figure 12 with $\Delta r = \Delta z = \Delta$ as the grid interval. This grid has the useful property that it has the minimum possible number of variables per grid cell.

We designate with V_{ij}^k the velocity variable in the (i, j) cell at time $k\Delta t$, and with $\Sigma_{ij}^{k+1/2}$ the stress variable in the same cell at time $(k+1/2)\Delta t$. Then we define the following
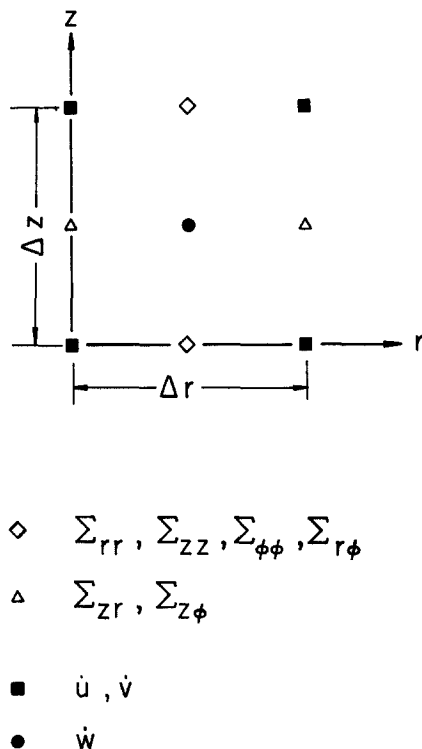

$$\diamond \quad \Sigma_{rr}, \Sigma_{zz}, \Sigma_{\phi\phi}, \Sigma_{r\phi}$$

$$\triangle \quad \Sigma_{zr}, \Sigma_{z\phi}$$

$$\blacksquare \quad \dot{u}, \dot{v}$$

$$\bullet \quad \dot{w}$$

FIG. 12. The finite difference grid used in the numerical solution of the circular fault. The grid is staggered in time so that the Σ_{ij} are defined at times $(k-1/2)\Delta t$ while $(\dot{u}, \dot{v}, \dot{w})$ are defined at $k\Delta t$.

centered difference operations

$$\Delta t \, \partial/\partial t \, V^{k+1/2} \to \delta_t V^{k+1/2} = V^k - V^{k-1}$$

$$\Delta \, \partial/\partial r \, V_{i+1/2,j} \to \delta_r V_{i+1/2,j} = V_{i,j} - V_{i-1,j}$$

$$\Delta \, \partial/\partial z \, V_{i,j+1/2} \to \delta_z V_{i,j+1/2} = V_{i,j} - V_{i,j-1}$$

$$\frac{V_{i+1/2}}{r} \to \frac{V_i + V_{i-1}}{2r} \tag{A3}$$

and similar operator for the derivatives of the stresses. In (A3) i, j and k may take the appropriate integer or half-integer values. We can then write the following difference equivalent of (A1).

$$\mathbf{V}^{k+1} = \mathbf{V}^k + H(\mathbf{A}\,\delta_r + \mathbf{B}\,\delta_z + \mathbf{C}\,\Delta/r)\,\Sigma^{k+1/2}$$

$$\Sigma^{k+1/2} = \Sigma^{k-1/2} + H(\mathbf{D}\,\delta_r + \mathbf{F}\,\delta_z + \mathbf{G}\,\Delta/r)\,\mathbf{V}^k. \tag{A4}$$

Where $H = \Delta t/\Delta$ is the time-space ratio of the grid. The problem is then to solve (A4) with (A2) as boundary conditions. The initial conditions are taken as $\mathbf{V}^0 = \Sigma^0 = 0$ everywhere. The boundary conditions (A2) give the starting values (on the $j = 0$ line) for the explicit difference equations (A4). Notice that the stress conditions $\Sigma_4 = -\Sigma_5 = 1$ are applied at the lowermost side of the cell, while $\mathbf{V}_1 = \mathbf{V}_2 = 0$ are applied at the center of the cell. This produces a $\Delta/2$ misalignment of the fault, but the effect does not appear to be important. At $r = 0$ ($i = 0$) we use the symmetry conditions of the velocity and stress fields to generate the boundary conditions.

Stability at interior points. Let us derive now the conditions for stability at internal points in the grid. This is a necessary condition for the overall numerical stability but it is not sufficient in the presence of boundary conditions.

We compute stability by the usual methods (Kreiss, 1973). Let's define a Fourier component of the solution at $t = k\Delta t$ and $t = (k-1/2)\Delta t$

$$\mathbf{V}^k = \mathbf{V}' \exp\left(-ik_r r - ik_z z\right)$$

$$\Sigma^{k-1/2} = \Sigma' \exp\left(-ik_r r - ik_z z\right) \tag{A5}$$

where k_r and k_z are the components of the wavenumber vector. The linearity of the equations requires that

$$\mathbf{V}^{k+1} = \varepsilon\,\mathbf{V}' \exp\left(-ik_r r - ik_z z\right)$$

$$\Sigma^{k+1/2} = \varepsilon\,\Sigma' \exp\left(-ik_r r - ik_z z\right) \tag{A6}$$

where ε is a complex number. A necessary condition for stability is that $|\varepsilon| \leqq 1$. Inserting (A5) into (A4) we find

$$(\varepsilon - 1)\,\mathbf{V}' = \varepsilon\mathbf{P}\,\Sigma'$$

$$(\varepsilon - 1)\,\Sigma' = \mathbf{Q}\,\mathbf{V}' \tag{A7}$$

where $\mathbf{P}$ and $\mathbf{Q}$ are matrices whose elements are functions of k_r, k_z and Δ/r. We can combine the equations in (A7) to find

$$(\varepsilon - 1)^2\,\mathbf{U}' = \varepsilon\mathbf{P}\cdot\mathbf{Q}\mathbf{U}' \tag{A8}$$

This equation is an eigenvalue problem for ε whose solution is straightforward but requires extensive algebra. We shall give a solution assuming that Δ/r is small and keeping terms of $0(\Delta/r)$. We find

$$(\varepsilon_l - 1)^2/\varepsilon_l = -4\kappa_l H^2(A + iB) \tag{A9}$$

where

$$A = \sin^2 k_r\,\Delta/2 + \sin^2 k_z\,\Delta/2,$$

$$B = \Delta/4r \sin k_r\,\Delta$$

and κ_l is a number such that $\kappa_1 = 1$ and $\kappa_2 = \kappa_3 = 1/3$. To each of these numbers corresponds a solution ε_l. The eigenvalue ε_1 corresponds to the P waves while ε_2 and ε_3 are associated with the two types of S waves in cylindrical coordinates. In order to find ε_l from (A9) we write

$$\varepsilon_l = \exp\left(i\omega_l\Delta t - \psi_l\right) \tag{A10}$$

where we have purposely written $\omega_l \Delta t$ to indicate that this imaginary exponent is associated with the propagation of the solution. The solution is

$$\cos \omega_l \Delta t = 1 - 2\kappa_l H^2 A$$

and

$$\psi_l = 2\kappa_l H^2 \frac{\Delta}{r} \frac{\sin k_r \Delta}{\sin \omega_l \Delta t}. \tag{A11}$$

The condition for stability is that $\omega_l \Delta t$ be real, this requires that $|1 - 2\kappa_l H^2 A| \leq 1$ for all possible values of k_r and k_z. The least favorable case is $k_r \Delta = k_z \Delta = \pi/2$, i.e., the Nyquist frequency for the grid. At that point $A = 2$ so that

$$H \leq \max \frac{\kappa_l}{\sqrt{2}} = 1/\sqrt{2}. \tag{A12}$$

This is the usual Courant–Friedrichs–Levy stability condition for a two-dimensional wave equation.

Dispersion and geometrical spreading. Inserting (A10) into (A6) we get

$$\mathbf{V}^{k+1} = \mathbf{V}_l \exp [i(\omega_l \Delta t - k_r \Delta - k_z \Delta) - \psi_l] \tag{A13}$$

where $\mathbf{V}_l$ is the projection of $\mathbf{V}'$ on the eigenvector of (A7) associated with ε_l. This form of the equation emphasizes the fact that ω_l is the frequency of the wave. From (A11) we find the following dispersion relation for ω_l.

$$\sin^2 \omega_l \Delta t/2 = \kappa_l H^2 (\sin^2 k_r \Delta/2 + \sin^2 k_z \Delta/2). \tag{A14}$$

For small k_r, k_z, and ω_l, (A14) reduces to the continuum dispersion relation

$$\omega_l = \kappa_l \sqrt{k_r^2 + k_z^2} = \kappa_l k \tag{A15}$$

which shows that κ_l is the square of the P or S velocity and that for long waves our numerical solutions approximate the exact solutions. It is interesting to note that (A14) is the dispersion relation found by Alford *et al.* (1974) for the explicit finite difference approximation of the second-order elastic-wave equation.

Finally note that ψ_l is related to the geometric spreading of cylindrical elastic waves. When the waves propagate outward ($k_r > 0$), $\psi_l < 0$ and, vice versa when $k_r < 0$, this is a physical effect unrelated to the stability of the numerical method.

Verification against an exact solution. The analysis above is valid only for points in the interior of the grid. Although this is a necessary condition for the stability of the numerical scheme, it tells nothing about the stability in the presence of the complicated boundary conditions at the fault. The only way to verify the stability is by comparison with analytical solutions. We tested the numerical method against Kostrov's (1964) solution of the self-similar circular shear crack given by equation (14). In Figure 13 we present a comparison between the exact and the numerical solution for the slip velocity at two points on the fault: at the center $r' = 0$ and midway along the final radius $r' = 0.5$. In the numerical results in the figure as well as in the other solutions in the main text, we used 20 points in the final fault radius ($\Delta = 0.05$) and $H = \Delta t/\Delta = 0.5$. Artificial dissipation was used to attenuate wavelengths close to the Nyquist frequency. The effect of the dissipation is visible especially in the solution at $r' = 0.5$ which tends to oscillate near the passage of the rupture front at $t = 1$. This oscillation is intrinsic to the problem since the continuous motion of the fault edge is being approximated by finite jumps in the grid. We consider this numerical solution to be accurate down to wavelengths of about four or five grid intervals. This test is especially significant because the self-similar ·problem has no intrinsic length scale, so that the numerical solution would not improve
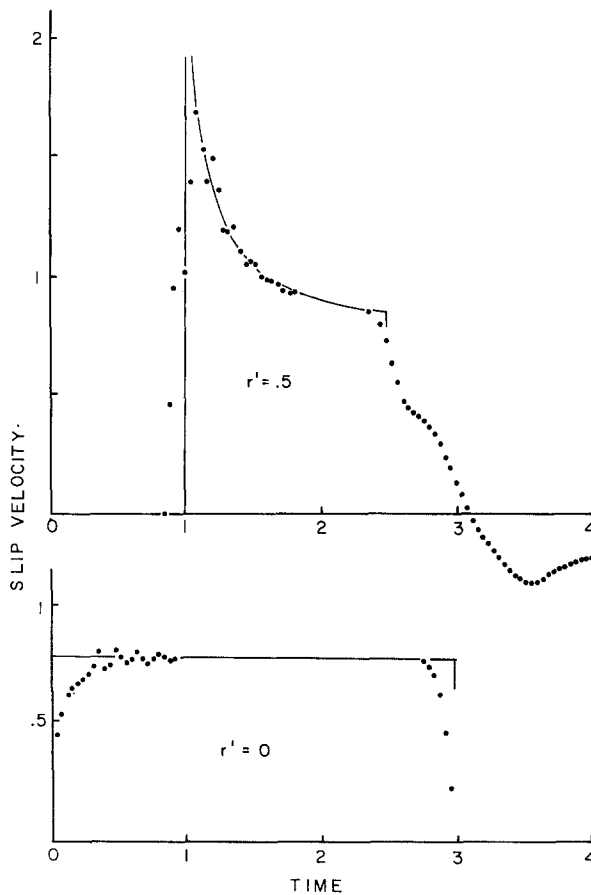
FIG. 13. A comparison of our numerical solution for the source slip velocity with the self-similar circular fault of Kostrov (1964). The analytical solution is valid only until the arrival of the P stopping phases. The arrival of the stopping phases is indicated by the interruption of the analytical solution. We compare the slip velocities at center of the fault ($r = 0$) and at $r = 0.5a$. Slip was not stopped by friction in this example and negative slip velocities are shown at $r = 0.5a$. The numerical solution near the singular rupture front at $t' = 1$, $r' = 0.5$ oscillates due to the discretization of the motion of the edge of the fault. This oscillation is attenuated by artificial damping of the numerical solution.

by the usual expedient of increasing the number of grid points. We also tested the solution against the statistic solutions of Keilis-Borok and verified that the behavior near the wave fronts is of the type predicted by diffraction theory.

References

Aki, K. (1966). Generation and propagation of G waves from the Niigata earthquake of June 16, 1964, 2, Estimation of earthquake moment, released energy, and stress-strain drop from G-wave spectrum, *Bull. Earthquake Res. Inst., Tokyo Univ.* **44**, 73–88.

Aki, K. (1967). Scaling law of seismic spectrum, *J. Geophys. Res.*, **72**, 1217–1231.

Aki, K. (1972). Earthquake mechanism, *Tectonophysics* **13**, 423–446.

Alford, R. M., K. R. Kelly, D. M. Boore (1974). Accuracy of finite-difference modelling of the acoustic wave equation, *Geophysics* **39**, 834–842.

Andrews, D. J. (1975). From anti-moment to moment: plane-strain models of earthquakes that stop, *Bull. Seism. Soc. Am.* **65**, 163–182.

Brune, J. N. (1970). Tectonic stress and the spectra of seismic shear waves from earthquakes, *J. Geophys. Res.* **75**, 4997–5009.

Burridge, R. (1969). The numerical solution of certain integral equations with non-integrable kernels arising in the theory of crack propagation and elastic wave diffraction, *Phil. Trans. Roy. Soc. London, Ser. A.* **265**, 353.

Burridge, R. (1973). Admissible speeds for plane-strain self-similar shear cracks with friction but lacking cohesion, *Geophys. J.* **35**, 439–455.

Burridge, R. and L. Knopoff (1964). Body force equivalents for seismic dislocations, *Bull. Seism. Soc. Am.* **54**, 1875–1888.

Burridge, R. and C. Levy (1974). Self-similar circular shear cracks lacking cohesion, *Bull. Seism. Soc. Am.* **64**, 1789–1808.

Burridge, R. and J. Willis (1969). The self-similar problem of the expanding elliptical crack in an anisotropic solid, *Proc. Camb. Phil. Soc.* **66**, 443–468.

Dahlen, F. A. (1974). On the ratio of P-wave to S-wave corner frequencies for shallow earthquake sources, *Bull. Seism. Soc. Am.* **64**, 1159–1180.

Dieterich, J. H. (1973). A deterministic near-field source model, *Proc. World Conf. Earthquake Eng., 5th, Rome.*

Freund, L. B. (1972a). Crack propagation in an elastic solid subjected to general loading, *J. Mech. Phys. Solids* **20**, 129.

Freund, L. B. (1972b). Energy flux into the tip of an extending crack in an elastic solid, *J. Elasticity*, **2**, 341–348.

Hamano, Y. (1974). Dependence of rupture-time history on the heterogeneous distribution of stress and strength on the fault plane, *EOS. Trans. Am. Geophys. Union* **55**, 362.

Hanson, M. E., A. R. Sanford, and R. J. Shaffer (1971). A source function for a dynamic bilateral brittle shear failure, *J. Geophys. Res.* **76**, 3375–3383.

Haskell, N. A. (1964). Total energy and energy spectral density of elastic wave radiation from propagating faults, *Bull. Seism. Soc. Am.* **54**, 1811–1841.

Ida, Y. (1973). Stress concentration and unsteady propagation of longitudinal shear cracks. *J. Geophys. Res.* **78**, 3418–3429.

Keilis-Borok, V. I. (1959). On the estimation of the displacement in an earthquake source and of source dimensions, *Ann. Geofis.* **12**, 205–214.

Kostrov, B. V. (1964). Self-similar problems of propagation of shear cracks, *J. Appl. Math. Mech.* **28**, 1077–1087.

Kostrov, B. V. (1966). Unsteady propagation of longitudinal shear cracks, *J. Appl. Math. Mech.* **30**, 1241–1248.

Kostrov. B. V. (1974a). Seismic moment and energy of earthquakes, and seismic flow of rock, *Izv. Fizika Zemli* **1**, 23–40.

Kostrov, B. V. (1974b). Crack propagation at variable velocity, *J. Appl. Math. Mech.* **38**, 511–519.

Kostrov, B. V., L. V. Nikitin, and L. M. Flitman (1970). Mechanics of brittle fracture, *Izv. Akad. Nauk SSSR, Mekh. Tverd. Telo.* **3**.

Kreiss, H. and J. Oliger (1973). Methods for the approximate solution of time dependent problems, GARP publications, series No. 10, W.M.O. Geneva, Switzerland.

Madariaga, R. (1974). Seismic radiation from dynamic frictional faulting models, (abstract), *EOS* **56**, 1147.

Molnar, P., B. Tucker, and J. N. Brune (1973). Corner frequencies of P and S waves and models of earthquake sources, *Bull. Seism. Soc. Am.* **65**, 2091–2104.

Richards, P. G. (1973). The dynamic field of a growing plane elliptical shear crack, *Intern. J. Solids Structures* **9**, 843–861.

Rychtmyer, R. and K. Morton (1967). *Difference methods for initial value problems*, 2nd ed., Interscience Publishers, New York.

Savage, J. C. (1966). Radiation from a realistic model of faulting, *Bull. Seism. Soc. Am.* **56**, 577–592.

Savage, J. C. (1972). Relation of corner frequency of fault dimensions *J. Geophys. Res.* **77**, 3788–3795.

Savage, J. C. (1974). Relation between P and S corner frequencies in the seismic spectrum, *Bull. Seism. Soc. Am.* **64**, 1621–1627.

Savage, J. C. and M. D. Wood (1971). The relation between apparent stress and stress drop, *Bull. Seism. Soc. Am.* **61**, 1381–1388.

Thatcher, W. and T. C. Hanks (1973). Source parameters of Southern California earthquakes, *J. Geophys. Res.* **78**, 8547–8576.

Wyss, M. and P. Molnar (1972). Efficiency, stress drop, apparent stress, effective stress and frictional stress of Denver, Colorado earthquakes, *J. Geophys. Res.* **77**, 1433–1438.

DEPARTMENT OF EARTH AND PLANETARY SCIENCES
MASSACHUSETTS INSTITUTE OF TECHNOLOGY 54-514
CAMBRIDGE, MASSACHUSETTS 02139